OPEN ACCESS
IOP Publishing
Classical and Quantum Gravity
Class. Quantum Grav. **42** (2025) 015007 (24pp) https://doi.org/10.1088/1361-6382/ad942d

Realistic binary neutron star initial data with `Elliptica`

Alireza Rashti[1,2,*] **and Andrew Noe**[1,2]

[1] Institute for Gravitation & the Cosmos, The Pennsylvania State University, University Park, PA 16802, United States of America
[2] Department of Physics, The Pennsylvania State University, University Park, PA 16802, United States of America

E-mail: numerical.relativity@gmail.com

Received 19 July 2024; revised 3 November 2024
Accepted for publication 18 November 2024
Published 12 December 2024

Abstract

This work introduces the `Elliptica` pseudo-spectral code for generating initial data of binary neutron star systems. Building upon the recent `Elliptica` code update, we can now construct initial data using not only piecewise polytropic equations of state, but also tabulated equations of state for these binary systems. Furthermore, the code allows us to endow neutron stars within the binary system with spins. These spins can have a magnitude close to the mass shedding limit and can point in any direction.

Keywords: initial data, binary neutron star, elliptic solver, equation of state

1. Introduction

Binary neutron star (BNS) systems are very common in our Universe. Estimates suggest their merger rate falls between 250–2810 $\mathrm{Gpc}^{-3}\mathrm{yr}^{-1}$ [1]. The coalescence of these BNS systems is a source of myriad phenomena such as, among others, ejecta [2, 3], accretion disk [4], jets [5], r-process nucleosynthesis [6], and kilonova [7]. These phenomena are treasure trove of information revealing aspects of physics at large scales, for instance, gravity in strong regimes and physical constants of the Universe, as well as aspects of physics regarding small scales, like, equation of state (EOS) in supranuclear dense matter and formation of heavy elements in the periodic table.

* Author to whom any correspondence should be addressed.

As such, current detectors such as LIGO [8], VIRGO [9], and KAGRA [10] and the next generation ones like Cosmic Explorer [11], the Deci-hertz Interferometer Gravitational-wave Observatory [12], Einstein Telescope [13], LIGO Voyager [14], the laser interferometer space antenna [15], NEMO [16], and TianQin [17] are designed to look eagerly into sky and observe the physical signals emitted from the coalescence of compact binaries.

To unlock the wealth of information encoded in gravitational waves and their electromagnetic counterparts, accurate theoretical models are crucial. These models are essential for understanding events like GW170817 [18], the short gamma-ray burst GRB170817A [19], and the kilonova transient AT2017gfo [20]. However, finding analytical solution of the governing partial differential equations (PDEs), when BNS systems are coalescing, is not feasible as the PDEs are in a highly non-linear regime where no approximation is applicable [21]. In light of this, numerical relativity (NR) community have put significant efforts to solve these equations numerically and hence make sense of the observations.

Simulation of compact binary system in NR often involves two steps. The first step is to find the solution of Einstein–Euler PDEs on a hypersurface of the spacetime manifold, namely, constructing constraint satisfying and self-consistent initial data (ID) that present the binary system of interest at some time. ID codes such as, `COCAL` [22–24], `Elliptica` [25], `FUKA` [26], `LORENE` [27–31], `NRPyElliptic` [32], `SGRID` [33–35], `SpECTRE`'s elliptic solver [36, 37], `Spells` [38–41], `TwoPunctures` [42, 43], are developed and utilized for this step.

The next step is to use the ID and simulate the system's evolution over time; hence we can find the solution over the spacetime of interest. Dynamical evolution codes, for instance, `AthenaK` [44, 45], `BAM` [46–48], `BAMPS` [49–51], `Dendro-GR` [52], `Einstein Toolkit` [53, 54], `ExaHyPE` [55] `GR-Athena++` [56–58] `GRaM-X` [59, 60], `GRChombo` [61, 62], `Nmesh` [63], `NRPy+` [64], `SACRA-MPI` [65], `Simflowny` [66], `SpEC` [67, 68], `SpECTRE` [69, 70], and `SPHINCS_BSSN` [71], among others, are made and employed for this step.

Previously, `Elliptica` [25] was limited to the construction of ID for black hole neutron star (NS) binary systems. Additionally, the code was only supporting polytropic or piecewise polytropic EOSs. In this work, we extend `Elliptica`'s infrastructure to construction ID for BNS systems as well as supporting tabulated EOSs, for instance, the `CompOSE` tables [72–74].

To this aim, the Einstein–Euler equations are cast into coupled non-linear elliptic PDEs [34, 75, 76], and solved iteratively using Newton–Raphson method by the Schur domain decomposition [25]. During the solve, the cubed spherical patches adapt to the surface of the NSs thus separating matter and vacuum and preventing Gibbs phenomena in the spectral method. To achieve the target values of interest such as momenta of the system, mass and center of NSs, they are checked and adjusted during the solve. The EOSs are approximated by either (piecewise) polytropic or tabulate ones.

The remainder of paper is organized as follows. In section 2 we explain the mathematical background and formalism we use for ID of BNS systems, in particular, Einstein–Euler equations and EOS in `Elliptica`. Section 3 details the underling algorithms and numerical techniques for construction of BNS's ID. We present the implementation of tabulated EOS by spline interpolant means and diagnostics in `Elliptica`. Additionally, we explain the iterative procedure for finding the physical and constraint satisfying ID for BNS systems. In section 4, we present various convergence tests and comparison against post Newtonian answers to showcase the proof of concept for the new version the code. In section 5, we discuss the possible improvements and future work.

Throughout the article, we use geometric units where $G = 1$ is the constant of gravity, $c = 1$ is the speed of light, and solar mass $M_\odot = 1$. Additionally, following [77], we absorb the speed of light c in the definition of pressure and total energy density.

2. Formalism

2.1. Einstein–Euler equations

To derive the equations that govern the gravity and matter on a spatial-like hypersurface Σ_t of a four-dimensional manifold $\mathcal{M}$ with a metric $g_{\mu\nu}$, we first write the line element of $\mathcal{M}$ as

$$\mathrm{d}s^2 = g_{\mu\nu}\mathrm{d}x^\mu dx^\nu = -\alpha^2\mathrm{d}t^2 + \gamma_{ij}\left(\mathrm{d}x^i + \beta^i\,\mathrm{d}t\right)\left(\mathrm{d}x^j + \beta^j\mathrm{d}t\right). \tag{1}$$

This specific form of the line element is particularly well-suited for the $3+1$ formalism. It provides a clear view of the key variables (fields): α, β^i, and γ_{ij}. Here, α is the lapse gauge and indicates the way that a sequence of spatial slices, Σ_ts, are combined to form the complete spacetime manifold M. γ_{ij} is the induced three-metric on each spatial hypersurface and can be written as $\gamma_{\mu\nu} = g_{\mu\nu} + n_\mu n_\nu$, where n^μ is the normal vector on Σ_t. β^i is the shift vector. The importance of this gauge, i.e. shift vector, is that it represents the coordinate frame being used in each hypersurface. In this work, we take the shift vector as follows

$$\beta^i = B^i + \epsilon_{ijk}\Omega^j_{\mathrm{BNS}}\left(r^k - r^k_{\mathrm{CM}}\right) + \frac{v_r}{r_{\mathrm{BNS}}}\left(r^i - r^i_{\mathrm{CM}}\right). \tag{2}$$

Here, Ω^i_{BNS} is the orbital angular velocity of the BNS system, r^i_{CM} is the position of the system's center of mass, r_{BNS} is the coordinate distance between the NS centers, v_{r} is the radial velocity of the inspiraling coordinate system, and ϵ_{ijk} is the Levi-Civita symbol. Equation (2) proves numerically convenient when applying boundary condition (BC) for β^i at the edge of the computational grid where the position vector $\vec{r}$ has large values.

By definition the extrinsic curvature on Σ_t is $K_{\mu\nu} = -\frac{1}{2}\pounds_n\gamma_{\mu\nu}$, in which $\pounds_n$ is the Lie derivative along the normal vector. We note that by construction $K_{\mu\nu}n^\mu = 0$, therefore, we can use spatial indices to describe the extrinsic curvature. Next, by utilizing conformal decomposition, we write

$$\gamma_{ij} = \psi^4\bar{\gamma}_{ij}, \tag{3}$$

$$K^{ij} = A^{ij} + \frac{1}{3}K\gamma^{ij}. \tag{4}$$

Here ψ is the conformal factor, $\bar{\gamma}_{ij}$ the conformal three-metric, A^{ij} the traceless part of K^{ij}. Moreover, since we are using the extended conformal thin sandwich (XCTS) formalism [75, 76]

A^{ij} is decomposed as

$$A^{ij} = \psi^{-10}\bar{A}^{ij}, \tag{5}$$

$$\bar{A}^{ij} = \frac{1}{2\bar{\alpha}}\left((\bar{L}\beta)^{ij} - \bar{\gamma}^{ik}\bar{\gamma}^{jl}\bar{u}_{kl}\right), \tag{6}$$

where

$$\bar{u}_{ij} = \frac{\partial\bar{\gamma}_{ij}}{\partial t}, \tag{7}$$

$$(\bar{L}\beta)^{ij} = \bar{D}^i\beta^j + \bar{D}^j\beta^i - \frac{2}{3}\bar{\gamma}^{ij}\bar{D}_k\beta^k, \tag{8}$$

$$\alpha = \psi^6\bar{\alpha}, \tag{9}$$

and $\bar{D}$ is the covariant derivative compatible with $\bar{\gamma}_{ij}$.

To complete the formulation we need to incorporate the source terms. We assume the fluid in NSs are governed by ideal fluid, hence the stress energy tensor can be written as

$$\begin{aligned} T_{\mu\nu} &= (\rho_0 + \rho_0\epsilon + P)\, u_\mu u_\nu + P g_{\mu\nu}, \\ &= \rho_0 h u_\mu u_\nu + P g_{\mu\nu}, \end{aligned} \tag{10}$$

where, ρ_0 is the rest mass density, ϵ the specific internal energy, P the pressure, h the specific enthalpy, and u^μ the four-velocity of the fluid. Additionally, for $3+1$ decomposition purposes, we project the stress energy tensor with respect to Σ_t as follows

$$E = n_\mu n_\nu T^{\mu\nu}, \tag{11}$$

$$S = \gamma^{ij}\gamma_{i\mu}\gamma_{j\nu}T^{\mu\nu}, \tag{12}$$

$$j^i = -\gamma^i_\mu n_\nu T^{\mu\nu}, \tag{13}$$

where, E is the measured energy by the Eulerian observer whose four-velocity is n^μ. S is the trace of matter stress tensor, and j^i is the momentum flux.

Unique answer to a linear elliptic equation with a source is guaranteed by the maximum/minimum principle. This principle becomes important during solve of constraint equations for high mass NSs (for further discussion see [78]). To maintain the maximum/minimum principle, we rescale the stress energy projections as

$$E = \psi^{-6}\bar{E}, \tag{14}$$

$$S = \psi^{-6}\bar{S}, \tag{15}$$

$$j^i = \psi^{-6}\bar{j}^i. \tag{16}$$

Finally, following XCTS formalism, we write Einstein's equations in quasi equilibrium condition

$$\bar{D}^2\psi - \frac{1}{8}\psi\bar{R} - \frac{1}{12}\psi^5 K^2 + \frac{1}{8}\psi^{-7}\bar{A}_{ij}\bar{A}^{ij} + 2\pi\psi^{-1}\bar{E} = 0, \tag{17}$$

$$\begin{aligned} &\bar{D}^2\left(\bar{\alpha}\psi^7\right) - \left(\bar{\alpha}\psi^7\right)\left[\frac{1}{8}\bar{R} + \frac{5}{12}\psi^4 K^2 + \frac{7}{8}\psi^{-8}\bar{A}_{ij}\bar{A}^{ij}\right] \\ &\quad + \psi^5\left(\partial_t K - \beta^k\partial_k K\right) - 2\pi\bar{\alpha}\psi^5\left(\bar{E} + 2\bar{S}\right) = 0, \end{aligned} \tag{18}$$

$$2\bar{\alpha}\left[\bar{D}_j\left(\frac{1}{2\bar{\alpha}}\left(\bar{L}\beta\right)^{ij}\right) - \bar{D}_j\left(\frac{1}{2\bar{\alpha}}\bar{u}^{ij}\right) - \frac{2}{3}\psi^6\bar{D}^i K\right] - 16\pi\bar{\alpha}\psi^4\bar{j}^i = 0, \tag{19}$$

with the BCs

$$\lim_{r\to\infty}\psi = 1, \quad \lim_{r\to\infty}B^i_0 = 0, \quad \lim_{r\to\infty}\alpha\psi = 1. \tag{20}$$

Additionally, we pick the free data as

$$\bar{\gamma}_{ij} = \delta_{ij}, \tag{21}$$

$$K = 0, \tag{22}$$

$$\bar{u}_{ij} = 0. \tag{23}$$

For hydrodynamic equations, following [34], we decompose the fluid into two parts: the rotational part of the fluid and is represented by a cross product, and the irrotational part of

the fluid that is represented by a velocity potential (see, e.g. [79]). In particular, the rotational part, which represents the NS spin, reads

$$w^i = \epsilon_{ijk}\Omega^j_{\rm NS}\left(x^k - x^k_{\rm c}\right), \tag{24}$$

here, $\Omega^j_{\rm NS}$ is a free parameter to set the spin level, see section 4.3, and $x^k_{\rm c}$ denotes the NS coordinate. The irrotational part is shown by the potential $\phi(x,y,z)$ and obeys the following equations [35].

$$\begin{aligned}&\frac{c\left(\rho_0\right)\alpha}{h}\psi^{-4}\bar{\gamma}^{ij}\partial_i\partial_j\phi - \frac{\rho_0\alpha}{h}\psi^{-4}\bar{\gamma}^{ij}\bar{\Gamma}^k_{ij}\partial_k\phi + 2\frac{\rho_0\alpha}{h}\psi^{-5}\bar{\gamma}^{ij}\left(\partial_i\psi\right)\left(\partial_j\phi\right)\\ &\quad + \left(D_i\frac{\rho_0\alpha}{h}\right)\left(D^i\phi\right)D_i\left[\frac{\rho_0\alpha}{h}w^i - \rho_0\alpha u^0\left(\beta^i + \xi^i\right)\right] = 0,\end{aligned} \tag{25}$$

where, ∂_i denotes the spatial partial derivative with respect to Cartesian coordinate x^i and ξ^i is the Killing vector. Here, following the smoothing method in [35]

$$c\left(\rho_0\right) = \rho_0 + \bar{\epsilon}\rho_{0\rm c}\left(\frac{\rho_{0\rm c} - \rho_0}{\rho_{0\rm c}}\right)^4, \tag{26}$$

in which, $\rho_{0\rm c}$ is the values of ρ_0 at the NS center, and $\bar{\epsilon}$ is a constant number—for which we generally use 0.1. Since the fluid is enclosed inside the patches that cover the NS, we further need to impose a BC on the NS surface as

$$D^i\phi D_i\rho_0 + w^i D_i\rho_0 - hu^0\left(\beta^i + \xi^i\right)D_i\rho_0 = 0. \tag{27}$$

We note that since equations (25) and (27) only include derivatives of ϕ, we can not uniquely determine ϕ. Hence, we further demand that the value of ϕ at the NS center is a constant number—like 0.

2.2. Equation of state

In order to close the system of equations we need an EOS. `Elliptica` deploys specific enthalpy, h, to create a link between the macroscopic properties of the matter and the gravity. As such, if we have a piecewise EOS we write

$$\begin{aligned}\rho_0\left(h\right) &= K_i^{-n_i}\left(\frac{h-1-a_i}{n_i+1}\right)^{n_i},\\ P\left(h\right) &= K_i^{-n_i}\left(\frac{h-1-a_i}{n_i+1}\right)^{n_i+1},\\ \epsilon\left(h\right) &= \frac{a_i + n_i\left(h-1\right)}{n_i+1},\end{aligned} \tag{28}$$

where $n_i = \frac{1}{\Gamma_i - 1}$ is the polytropic index and K_i's are specific to the given EOS; a_i's ensure the continuity of EOS [77] and are set as

$$\begin{aligned}a_0 &= 0,\\ a_i &= a_{i-1} + \frac{K_{i-1}}{\Gamma_{i-1}-1}\rho_i^{\Gamma_{i-1}-1} - \frac{K_i}{\Gamma_i - 1}\rho_i^{\Gamma_i - 1}.\end{aligned} \tag{29}$$

Similarly, for tabulated EOSs we represent $\rho_0\left(h\right)$, $P\left(h\right)$, and $\epsilon\left(h\right)$ as spline interpolants given discrete data points (ρ_0, P, ϵ, h). Although typically only the quantities (ρ_0, P, ϵ) or

(ρ_0, P, e) are provided in tables, where e is the total energy density, we may convert between variables via the relations:

$$\begin{aligned} e &= \rho_0 (1+\epsilon), \\ h &= 1+\epsilon+\frac{P}{\rho_0}. \end{aligned} \tag{30}$$

Having written thermodynamic variables in terms of specific enthalpy, we now write specific enthalpy in terms of the metric and fluid variables [34]

$$\begin{aligned} h &= \sqrt{L^2 - (D_i\phi + w_i)(D^i\phi + w^i)}, \\ L^2 &= \frac{b + \sqrt{b^2 - 4\alpha^4 \left[(D_i\phi + w_i) w^i\right]^2}}{2\alpha^2}, \\ b &= \left[\left(\xi^i + \beta^i\right) D_i\phi - C\right]^2 + 2\alpha^2 (D_i\phi + w_i) w^i. \end{aligned} \tag{31}$$

3. Numerical method

3.1. Coordinate system

The computation grid is tiled by cubed spherical coordinate systems [80], except at the NS centers, where we use simple Cartesian boxes to avoid coordinate singularities at $r = 0$ [25, 35]. The relation between Cartesian coordinate, denoted by $x^i = (x, y, z)$, and cubed spherical coordinate, $X^i = (X, Y, Z)$, is

$$X(x,y,z) = \frac{x}{z},\ Y(x,y,z) = \frac{y}{z},\ Z(x,y,z) = \frac{z - r_{\rm in}}{r_{\rm out} - r_{\rm in}}, \tag{32}$$

here, X and Y take value $\in [-1, 1]$, and $Z \in [0, 1]$. Additionally, $r_{\rm in}$ and $r_{\rm out}$ are defined

$$r_{\rm in} = \frac{\sigma_{\rm in}(X,Y)}{\sqrt{1+X^2+Y^2}},\ r_{\rm out} = \frac{\sigma_{\rm out}(X,Y)}{\sqrt{1+X^2+Y^2}}. \tag{33}$$

where, the shape of the inner boundary of a patch along the radial direction is determined by $\sigma_{\rm in}(X,Y)$ and its outer boundary by $\sigma_{\rm out}(X,Y)$. $\sigma(X,Y)$ is related to Cartesian coordinates by the equation $\sigma(X,Y) = \sqrt{x^2+y^2+z^2}$. Finally, we note that while equation (32) is written for patches along the z-axis, one can generalize this along any other axes.

As the distance from NSs increases, we expect the fields fall as powers of r^{-1}. To account for this behavior we use a new transformation for Z coordinate, denoted by $\widetilde{Z}$, for the paches covering large radii of the grid. The transformation reads

$$\widetilde{Z} = \frac{\sigma_{\rm out}}{\sigma_{\rm out} - \sigma_{\rm in}} \left(1 - \frac{\sigma_{\rm in}}{r}\right). \tag{34}$$

Here $r = \sqrt{x^2+y^2+z^2}$ and still $\widetilde{Z} \in [0, 1]$.

Finally, `Elliptica` uses Chebyshev polynomials of the first kind for the basis of the spectral expansion and deploys the extrema of Chebyshev polynomials for its collocation points [25].

Figure 1 illustrates the patches covering the x–y plane of the computational grid used in this work. It is worth noting that the sizes used for the grid and NS are reduced to illustrate the complete computational grid. In practice, we set the outer boundary at a radius of $10^5\,\mathrm{M}_\odot$.

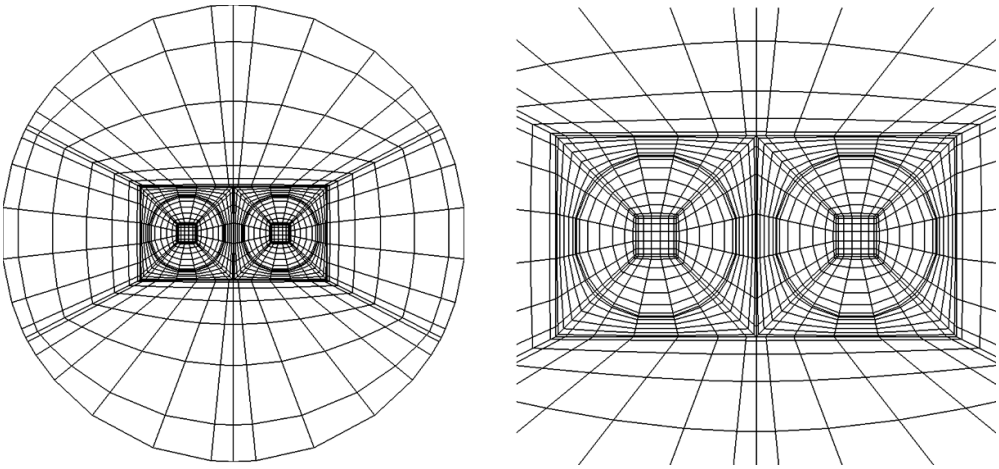

Figure 1. Grid patches for a BNS system. Left: shown is the x–y plane of the computational grid that is covered by different patches. To fully represent the grid, the other boundary is set to a shorter length. For a production run, the outer boundary is set generally at a radius of $10^5\,\mathrm{M}_\odot$ from to the center of grid. Right: a zoomed-in view of the x–y plane focusing on the NS regions. A Cartesian box is used around each NS center to avoid coordinate singularities. By using various $\sigma(X, Y)$ values, cubed spherical patches can adapt to different shapes, effectively capturing the shape of the NS surface. This allows for the treatment of matter and vacuum in separate patches.

3.2. Elliptic solver

Given an elliptic PDE, we linearize the equation to use the Newton–Raphson method (see [25] for a complete description). Thus, the original elliptic PDE becomes a matrix equation, like $Ax = B$, to be solved. Now the challenge is to solve this matrix equation efficiently. To this aim, we use the Schur domain decomposition method [25, 81]. At the core of this method there is a divide and conquer strategy; in this strategy, first the coupled equations are solved, and then the system decomposes into independent (uncoupled) subsystems, amenable for parallel solving. The Schur domain decomposition allows solving the full system using shared memory multiprocessing in which each CPU core is assigned to solve a matrix equations at each patch independently.

The Schur domain decomposition method arranges the Jacobian matrix in Newton–Raphson method into two parts. The first part is associated with all uncoupled equations and the second part comprises the coupled equations. These couplings between equations occur due to the inter-BC at the interfaces of adjacent patches [25]. As such, the system of matrix equations can be seen as two equations with two unknowns as follows

$$\begin{pmatrix} B & E \\ F & C \end{pmatrix} \begin{pmatrix} \tilde{v} \\ \tilde{w} \end{pmatrix} = \begin{pmatrix} f \\ g \end{pmatrix}, \tag{35}$$

where, the vector $\tilde{v}$ denotes all the unknowns that are uncoupled, i.e. $\tilde{v}$ comprises all unknowns that stem from inner points of a patch and hence uncoupled from the other patches. The vector $\tilde{w}$ is the unknowns that are due to coupled equations, i.e. stem from inter-BC between adjacent patches. By such an arrangement, if the unknown $\tilde{w}$ is solved, then the equation of $\tilde{v}$ can be solved consequently.

Algorithm 1. Schur complement domain decomposition method.

1: Solve $BE' = E$ for E';
2: Solve $Bf' = f$ for f';
3: Compute $g' = g - Ff'$;
4: Compute $S = (C - FE')$;
5: Solve $S\tilde{w} = g'$ for $\tilde{w}$;
6: Compute $\tilde{v} = f' - E'\tilde{w}$;

Therefore, we first solve for $\tilde{w}$, and then we use it to solve for $\tilde{v}$. Accordingly, in `Elliptica`, we solve equation (35) like:

$$(C - FE')\,\tilde{w} = g - Ff', \tag{36}$$

$$\tilde{v} = f' - E'\tilde{w}, \tag{37}$$

where

$$\begin{aligned} E' &= B^{-1}E, \\ f' &= B^{-1}f. \end{aligned} \tag{38}$$

As we can see equation (36) only involves the unknown $\tilde{w}$, and it can be summarized as

$$S\tilde{w} = g', \tag{39}$$

where, S is called Schur complement matrix.

After solving equation (39) for $\tilde{w}$, we solve for $\tilde{v}$ using equation (37) – hence we find the solution of the whole system.

A summary of the Schur complement domain method to solve elliptic equations is shown in algorithm 1. For a more in-depth discussion about implementation of Schur domain decomposition and parallelization of matrix solver the reader may consult [25]. Finally, we use the publicly available and open-source `UMFPACK` direct solver [82].

3.3. Diagnostics

In `Elliptica` we compute the baryon mass of each NS using [83]

$$M_B = \int_{\mathrm{NS}} \rho_0 \alpha \psi^6 \sqrt{\bar{\gamma}}\, \mathrm{d}^3x, \tag{40}$$

in which $\bar{\gamma}$ is the determinant of $\bar{\gamma}_{ij}$ and the integration is taken over the volume of the NS.

To measure the NS spins, we can use the flat space coordinate rotational Killing vector, following [84], on the surface of NS:

$$\begin{aligned} \vec{\phi}_x &= -(z - z_{\mathrm{c}})\,\vec{\partial}_y + (y - y_{\mathrm{c}})\,\vec{\partial}_z, \\ \vec{\phi}_y &= +(z - z_{\mathrm{c}})\,\vec{\partial}_x + (x - x_{\mathrm{c}})\,\vec{\partial}_z, \\ \vec{\phi}_z &= -(y - y_{\mathrm{c}})\,\vec{\partial}_x + (x - x_{\mathrm{c}})\,\vec{\partial}_y, \end{aligned} \tag{41}$$

in which $(x_{\mathrm{c}}, y_{\mathrm{c}}, z_{\mathrm{c}})$ is the coordinate center of the NS and $(\vec{\partial}_i)_{i\in\{x,y,z\}}$ are the basis vectors associated with the Cartesian coordinates. Accordingly, NS spin S_i, for the i direction, is measured on the surface of NS by

$$S_i = \frac{1}{8\pi} \oint_{\mathrm{NS}} \left(\vec{\phi}_i\right)^j s^k K_{jk} \mathrm{d}A, \tag{42}$$

where, s^k is the normal vector on the NS surface. The dimensionless spin is defined

$$\chi_i := \frac{S_i}{M_{\rm NS}^2}. \tag{43}$$

Additionally, following [35], we can first compute the angular momentum J_i, the center $R_{\rm c}^i$, and linear momentum P_i of the NS, and then calculate S_i as follows

$$S_i = J_i - \epsilon_{ijk} R_{\rm c}^j P_k. \tag{44}$$

Since the chosen free data $\bar{\gamma}_{ij}$ in equation (21) satisfies the quasi-isotropic gauge condition [83] and K in equation (22) meets the asymptotic maximal gauge condition [83], the ADM linear momentums and angular momentums of the system are defined [83]

$$P_i^{\infty} = \frac{1}{8\pi} \lim_{S_t \to \infty} \oint_{S_t} (K_{jk} - K\gamma_{jk}) \left(\vec{\partial}_i\right)^j s^k {\rm d}A, \tag{45}$$

$$J_i^{\infty} = \frac{1}{8\pi} \lim_{S_t \to \infty} \oint_{S_t} (K_{jk} - K\gamma_{jk}) \left(\vec{\phi}_i\right)^j s^k {\rm d}A, \tag{46}$$

here,

$$\begin{aligned}
\vec{\phi}_x &= -(z - z_{\rm CM})\,\vec{\partial}_y + (y - y_{\rm CM})\,\vec{\partial}_z, \\
\vec{\phi}_y &= +(z - z_{\rm CM})\,\vec{\partial}_x + (x - x_{\rm CM})\,\vec{\partial}_z, \\
\vec{\phi}_z &= -(y - y_{\rm CM})\,\vec{\partial}_x + (x - x_{\rm CM})\,\vec{\partial}_y.
\end{aligned} \tag{47}$$

Lastly, to calculate the total ADM mass of the system, we use [83]

$$M_{\rm ADM} = \int_{\Sigma_t} \left[\psi^5 E + \frac{1}{16\pi}\left(\bar{A}_{ij}\bar{A}^{ij}\psi^{-7} - \bar{R}\psi - \frac{2}{3}K^2\psi^5\right)\right]\sqrt{\bar{\gamma}}{\rm d}^3x. \tag{48}$$

3.4. Tabulated equations of state

We can import tabulated EOSs from the `CompOSE` repository [72–74]. A general `CompOSE` table is first restricted to $T = 0$. The baryon density n_b is converted to the rest mass density ρ_0 via the neutron mass m_n: $\rho_0 = m_n n_b$.

We numerically differentiate and interpolate the EOS table to generate a Hermite spline representation of the functions $\rho_0(h)$, $P(h)$, and $\epsilon(h)$ (see section (appendix A)). In practice, the logarithms of these quantities are actually used to generate the interpolants.

A number of slight modifications may be made to the EOS in preprocessing in order to make it more amenable to interpolation. These modifications are necessary for both the physical consistency of the EOS and to facilitate the convergence of the solution.

The first modification involves adjusting specific enthalpy at the NS surface for the EOS tables in which the specific enthalpy falls below 1. To this aim, at the minimum pressure, which we consider occurring at the beginning of the table, we scale all ρ_0 points by the multiplicative constant $\eta = h_{\rm min}$ corresponding to the lowest value of h in the table. Accordingly, h points are scaled by the value η^{-1}, i.e:

$$\begin{aligned}
&\rho_0 \to \eta\rho_0 \\
h = \frac{e+P}{\rho_0} &\to \frac{e+P}{\eta\rho_0} = \eta^{-1}h.
\end{aligned} \tag{49}$$

This alteration can be carried through to dynamical evolution codes by e.g. using the same EOS table or by scaling the rest-mass density, at the minimum pressure, by the same factor used in the preprocessing step.

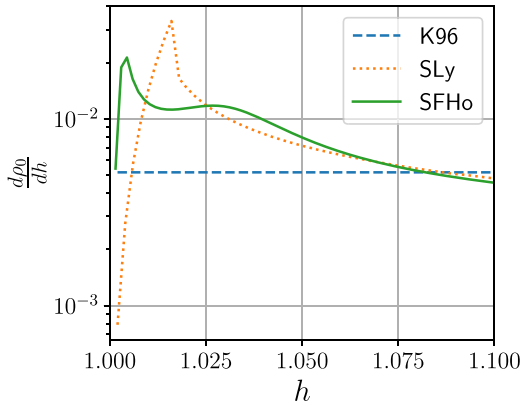

Figure 2. Comparison of changes with respect to the specific enthalpy (h) in the rest mass density (ρ_0) near the NS surface for three EOSs: K96 (single polytrope), SLy (piecewise polytrope), and SFHo (table). A lower specific enthalpy corresponds to a point closer to the NS surface, with $h = 1$ defining the surface itself. ρ_0 is in geometric unit and h is dimensionless.

In addition, several other features of tabular EOSs may pose problems for both interpolation and the use of specific enthalpy as the independent thermodynamic variable. Among these problems is the presence of a region near the surface of the NS where both $\frac{\mathrm{d}e}{\mathrm{d}h}$ and $\frac{\mathrm{d}\rho_0}{\mathrm{d}h}$ diverge. This region is common to many EOSs with a 'crust', including both tabular EOSs such as SFHo [85] and piecewise polytropics [86]. While this region is unavoidable if we wish to accurately represent the equation of state via specific enthalpy, see [87, 88], it also limits the accuracy of the solution within the NS (see figure 3).

Another consideration is the spacing of the data points in the `CompOSE` table, which may be highly irregular especially for tables generated as a piecewise combination of different models. To re-grid the EOS, we numerically differentiate the table points using Fornberg's method, explained in section (appendix B), and generate a low-degree Hermite interpolant, section (appendix A), which is sampled to produce new data points on an evenly-spaced grid. This method decreases oscillations when the new data points are themselves interpolated. Additionally, the interpolation of the EOS truncates the jumps in derivatives of the thermodynamic variables, i.e. $\frac{\mathrm{d}e}{\mathrm{d}h}$ and $\frac{\mathrm{d}\rho_0}{\mathrm{d}h}$, that as we mentioned before, in some tables are not well-defined. This low-degree Hermite interpolant corresponds to approximating the derivatives as finite at these points (since infinite values would be unphysical anyway).

Figure 2 shows the resultant tabulated SFHo EOS after re-griding using a low-degree Hermite interpolant with comparison to EOSs of K96 and SLy. The K96 EOS is a single polytrope, corresponding to $K = 96.7$ and $\Gamma = 2$ [89]. SLy is an approximate piecewise polytrope of tabulated SLy4, and therefore quantities such as $\frac{\mathrm{d}\rho_0}{\mathrm{d}h}$ are not continuous in certain regions corresponding to transitions between piecewise segments [90]. SFHo, here restricted to the zero-temperature regime, shows similar discontinuities [85].

Examining the functions relevant to the ID generation, e.g. ρ_0 and e, we see that the single-polytrope model is considerably simpler and more amenable to numerical solution than the models with discontinuities. The difference is typically relevant to the surface of the NS (where $h = 1$), as shown in the nearly vertical profile of $\frac{\mathrm{d}\rho_0}{\mathrm{d}h}$ in figure 2. The sharp changes in $\frac{\mathrm{d}\rho_0}{\mathrm{d}h}$ with the piecewise polytropic and tabular EOSs are not perfectly captured by the grid, and thus they limit the convergence of the constraint violations (see section 4.1).

There are several potential ways to improve the convergence properties of the code in this area. For example, one could apply filtering to the spectral coefficients [91] of ρ_0 or implement a routine to identify the location of discontinuities, thereby creating patches where the discontinuity occurs at the boundary between those patches. Additionally, using spectral EOS [87, 88, 92], and imposing continuity at the piecewise polytrope EOS [86] have been shown to enhance the continuity of the solutions. The implementation and comparison of these methods are left for future work.

3.5. ID construction

Construction of ID often necessitates an iterative approach. This process involves progressively refining the ID until a suitable solution is achieved. However, rapid or uncontrolled updates of the fields from one step to the next, or lack of adjustments of NS masses or their centers can lead to a divergent answer and code crashes. Another challenge is to find the NS surface after each update, as the true surface is unknown *a-priori*, and then creating a new computational grid with patch's surfaces adapted to the new NS surface.

We deploy the following iterative procedure to construct ID of a BNS system. In particular, we start from a coarse resolution grid and progressively refine the answer, while controlling diagnostics, until the Hamiltonian and momentum constraints, equations (55) and (56), reach a plateau. Then, we increase the resolution and repeat this iteration until we achieve the level of desired accuracy.

Step 0: we superimpose two Tolman–Oppenheimer–Volko (TOV) star solutions as the initial guess of the fields $\{\psi, \alpha\psi, B^i\}$. To initialize the ϕ fields for each NS we use the approximation $\phi = -\Omega^z_{\rm BNS}(y_{\rm NS} - y_{\rm CM})x$.

Step 1: We solve the elliptic equations iteratively in this specific order: first equation (25) for the matter field, and then equations (17)–(19) for the metric fields. This approach has been found to enhance the solution's stability, particularly when solving the matter field first. The order of solving the metric fields themselves, however, appears to be less critical. Moreover, during each iteration step, we focus on solving a single elliptic equation while keeping the other fields fixed. In essence, the fixed fields act as source terms influencing the equation being solved. Finally, within the Newton–Raphson iterative method, we perform only one update step per field, and then incorporating the newly solved value into the source terms for the next equation. In the following Ξ denotes a field from the set $\{\phi, \psi, \alpha\psi, B^i\}$.

Step 2: as mentioned earlier, iterative solvers are often sensitive to prompt changes; code crashes can happen if a sudden update take place in the system. As such, we update the field solutions that are obtained from *Step 1* in a relaxed fashion. To this aim, we use $\Xi = \lambda\Xi_{\rm new} + (1-\lambda)\Xi_{\rm old}$, in which $\Xi_{\rm old}$ denotes the solution before entering *Step 1* and $\Xi_{\rm new}$ is the solution after exiting that step. λ denotes the weight of update. We generally use $\lambda = 0.2$. This choice of λ value is proven to work for all experiments we have done.

Step 3: after updating all Ξ fields, we see the baryon mass of each NS deviates, often by a few percents, from the target value. Additionally, for spinning NSs, since at *Step 0* we used TOV solution, and then we added the spin vector to the NS, it is not surprising to observe the baryon mass is different from the prescribed target value. Moreover, the starting resolution is often coarse, and again the baryon mass may change as we go to a higher resolution. If we do not account for these changes, the baryon mass deviates even further at later iterations and may lead to a code crash. To adjust the baryon mass, we note that $\rho_0 = \rho_0(h)$, and as shown in equation (31) the specific enthalpy depends on a constant C, i.e. $h = h(C)$, which implies $\rho_0 = \rho_0(C)$. Therefore by using a root finder, we find the value of C in equation (40) such that the baryon mass remains the same as the target value.

Step 4: since at *Step 0* we began with a rough approximation of the solution, the linear ADM momentums are initially not zero. Furthermore, for asymmetric masses or spinning systems, we do not know in advance where is the exact position of the system center of mass—as one needs to consider the full general relativity effect to find it. Therefore, we iteratively find the system center of mass $\vec{r}_{\rm CM}$, by demanding the ADM momentum in each direction to be zero. The ADM momentum in z-direction proves consistently to be small, generally, $\frac{|P_z^\infty|}{M_{\rm ADM}} < 10^{-11}$, hence we keep $z_{\rm CM} = 0$, as the original value. However, often the initial value of ADM momenta in x or y direction is $\approx 10^{-5} M_{\rm ADM}$. Therefore, we adjust $x_{\rm CM}$ and $y_{\rm CM}$ as follows

$$\begin{aligned} x_{\rm CM,new} &= x_{\rm CM,old} + \lambda \frac{P_y^\infty}{\Omega^z_{\rm BNS} M_{\rm ADM}}, \\ y_{\rm CM,new} &= y_{\rm CM,old} - \lambda \frac{P_x^\infty}{\Omega^z_{\rm BNS} M_{\rm ADM}}. \end{aligned} \tag{50}$$

Here, λ is generally chosen 0.2. It is worth noting that K_{ij} is a function of β^i, while β^i through equation (2) is a function of $r^i_{\rm CM}$. Therefore, by adjusting the $r^i_{\rm CM}$, we influence K_{ij}—and hence all other fields as they are coupled to another—and we can derive P_i^∞ to zero iteratively.

Step 5: we update the stress energy tensor, in particular, we update the specific enthalpy for each NS in a relaxed fashion as $h = \lambda h_{\rm new} + (1-\lambda) h_{\rm old}$; λ is usually set to 0.5. Then, we use the new value of specific enthalpy to update $\rho_0(h)$, $\epsilon(h)$, and $P(h)$.

Step 6: finding the orbital angular velocity, $\Omega^z_{\rm BNS}$, for a quasi-circular orbit demands full solution of general relativity. Since we start with a Newtonian approximation for this value we need to refine it. Following [93], so called the force balance method, we first compute $\partial_i \ln\Gamma$ at each NS center, where Γ computed as

$$\Gamma = \frac{\alpha u^0 \left[1 - \left(\beta^i + \xi^i + \frac{w^i}{hu^0}\right) \frac{D_i \phi}{\alpha^2 h u^0} - \frac{w_i w^i}{(\alpha^2 h u^0)^2}\right]}{\sqrt{1 - \left(\beta^i + \xi^i + \frac{w^i}{hu^0}\right)\left(\beta_i + \xi_i + \frac{w_i}{hu^0}\right)\frac{1}{\alpha^2}}}. \tag{51}$$

Then, we use a root finder to find $\Omega^z_{\rm BNS}$ such that

$$\partial_i \ln\left[\alpha^2 - \left(\beta^i + \xi^i + \frac{w^i}{hu^0}\right)\left(\beta_i + \xi_i + \frac{w_i}{hu^0}\right)\right] + 2\partial_i \ln\Gamma = 0, \tag{52}$$

where, $\partial_i = \frac{\partial}{\partial x^i}$. Since in our setup the NS centers sit on y-axis, we compute equation (52) along this axis. We find $\Omega^z_{\rm BNS}$ for each NS centers and update it accordingly.

Step 7: at this point the specific enthalpy profile and hence NS surface are changed. We need to find the new location of NS surface for adjusting cubed spherical patches that are covering the NSs – so we can separate matter and vacuum into different patches. Since some parts of the NS may need to extend to the patches that are currently covering vacuum, we extrapolate h into these patches, so the root finder can find where $h = 1$. To this aim we use the following formula to extrapolate specific enthalpy to the vacuum

$$f(r) = \left(a + \frac{b}{r}\right) \exp\left(-c_0 \frac{r}{r_0}\right), \tag{53}$$

here, r denotes the coordinate distance from the NS center, and c_0 is a constant (typically 0.01). We find the values of a, and b by demanding C^1 continuity across the NS surface. Additionally, we use the same equation (53) to extrapolate ϕ field outside the NS. This step is required when the NS surface is expanded, and we want to interpolate ϕ from the current grid to a new grid.

Step 8: we identify the center of each NS by locating the coordinate where the specific enthalpy reaches its maximum value. After multiple updates to the matter fields in previous

steps, the NS centers can exhibit slight drifts from their initial positions. These drifts can accumulate over time, potentially leading to code crashes. To address this issue, we employ a corrective measure that adjusts the specific enthalpy function as follows

$$h_{\rm new}\left(\vec{r}\right) = h_{\rm old}\left(\vec{r}\right) - \left(\vec{r} - \vec{r}_0\right) \cdot \vec{\nabla} h_{\rm old}\left(\vec{r_0}\right), \tag{54}$$

where, r_0 denotes the coordinate of NS center. This adjustment ensures that the maximum value of the specific enthalpy remains at the same location, effectively preventing the NS centers from drifting significantly.

Step 9: we find the profile of $\sigma_{\rm out}(X, Y)$ that is necessary for equation (33) to have patch surfaces fitting the NS surface. To this end, for a given angular θ and ϕ in spherical coordinate, we use a root finder for r to solve $h(r, \theta, \phi) - 1 = 0$ and hence finding the new NS surface. Here, r is the coordinate distance from the NS center.

Step 10: if the NS surfaces are changed or if the resolution increases at the next iteration, we create a new grid. To ensure a smooth transition, we use spectral interpolation techniques to transfer data from the previous grid onto the new one.

Step 11: we monitor the Hamiltonian and momentum constraints, equations (55) and (56). We restart from *Step 1* unless the constraints reach their truncation error and are level off. In this case, when the constraints reach a plateau, we stop the iterative process if there is no higher resolution demanded; otherwise we go to the next resolution and start from *Step 1*.

4. Results

4.1. Convergence test

Since `Elliptica` is a pseudo-spectral code, the first expectation of the code is spectral convergence feature. As such, we calculate the Hamiltonian and momentum constraints, respectively, using

$$H := R - K_{ij}K^{ij} + K^2 - 16\pi E \tag{55}$$

$$M^i := D_j\left(K^{ij} - \gamma^{ij}K\right) - 8\pi j^i. \tag{56}$$

For the convergence test, we generate ID for two symmetric BNS systems: one with polytropic K96 EOS and the other with tabulated SFHo EOS. In these systems, the NSs have baryon mass 1.4 with no spin, and their separation is $50M_\odot$.

Figure 3 shows the L_2-norm of the Hamiltonian and momentum constraints as a function of grid resolution (focusing on the final iteration at each resolution) for the two systems. In figures 3(a) and (b)), the convergence test emphasizes on the NS. We observe the constraint violations decrease exponentially for smooth matter field, i.e. K96 EOS. For the SFHo EOS, initially for low resolutions the constraints converge exponentially but for higher resolutions the constraints level off. This behavior is expected; when the grid resolution is coarse the true discontinuities of EOS variables are not seen by the spectral expansion. For fine resolutions all features of EOS variables emerge and while spectral convergence try to resolve these features, but it is not successful. Hence, we see constraints are soon level off and do not decrease as we increase the resolution. We note that, for the tabular EOS (SFHo), the convergence is limited due to the sharp features of $\frac{{\rm d}\rho_0}{{\rm d}h}$ near the surface of the NS (see figure 2). Indeed, the overall magnitude of the constraint violations is higher and the rate of convergence is not exponential with the tabular EOS (in contrast to the simple polytrope). Nonetheless, the profile of the convergence tests still suggest convergence up to a limit at high resolutions.

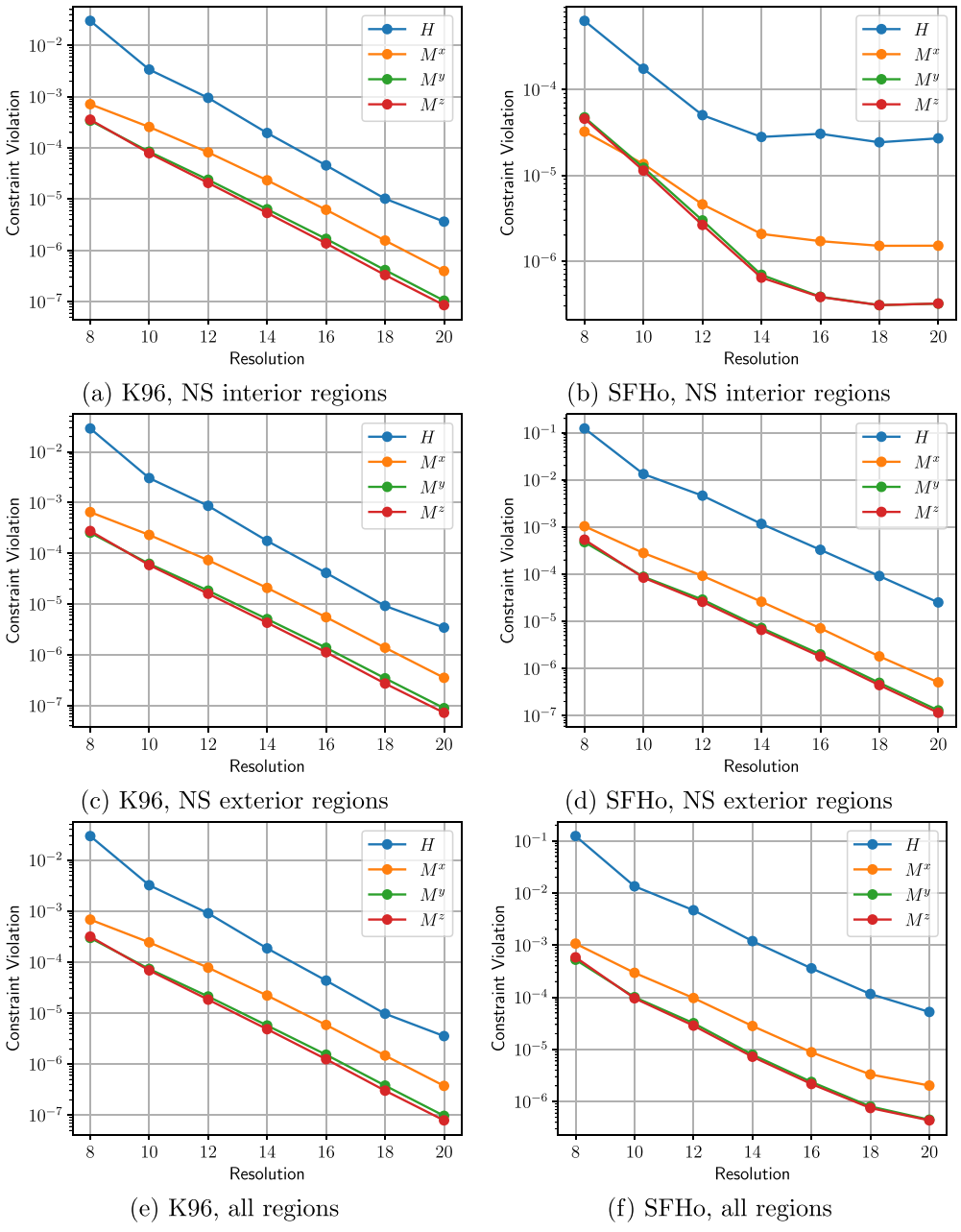

(a) K96, NS interior regions

(b) SFHo, NS interior regions

(c) K96, NS exterior regions

(d) SFHo, NS exterior regions

(e) K96, all regions

(f) SFHo, all regions

Figure 3. The L_2-norm of the Hamiltonian and momentum constraint violations for the BNS system with the K96 EOS (single polytrope) and the SFHo EOS (table). The constraint violations at each point are summed over all points in the specified regions. The regions not including a tabular EOS show exponential convergence, while regions with such an EOS reach a limit at high resolutions.

Ensuring spectral convergence of the code for regions that fields are smooth, we calculate L_2-norm of constraints at immediate neighboring regions of NSs, where there is no matter fields. Figures 3(c) and (d) demonstrates they convergence spectrally.

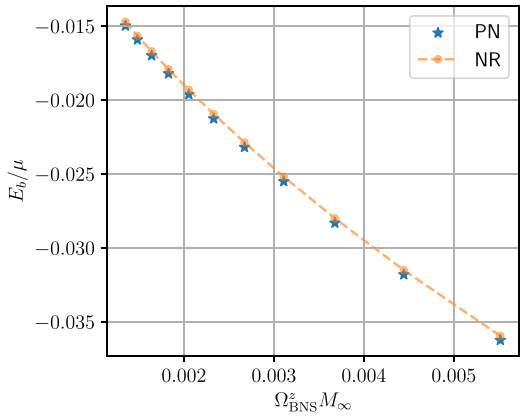

Figure 4. Analytic post-Newtonian (PN) curve versus NR curve. The values of E_b for given $\Omega^z_{\rm BNS}$ are compared for post-Newtonian method and NR method. For binaries with a large separation post-Newtonian and NR values are matching. For BNS of a close separation there is a slight deviation from post-Newtonian prediction as the system is not fully in quasi-circular status. Here, $\mu = M^1_{\rm TOV} M^2_{\rm TOV}/M_\infty$ and the binary has a symmetric baryon mass of 1.4 for each NS and uses tabulated SLy4 EOS.

Finally, the overall converge of the constraints, calculated over all regions, are shown in figures 3(e) and (f); while both systems exhibit convergence as the resolution increases, the rate of convergence for BNS with SFHo EOS is smaller than K96 EOS.

4.2. Post-Newtonian test

We calculate the binding energy $E_{\rm b}$ of a symmetric non-spinning BNS system with NS baryon mass 1.4 and tabulated SLy4 EOS for varied separations of NSs. Here $E_{\rm b} = M_{\rm ADM} - M_\infty$ and $M_\infty = M^1_{\rm TOV} + M^2_{\rm TOV}$; we use equation (48) to calculate $M_{\rm ADM}$ and $M^{1/2}_{\rm TOV}$ are the corresponding gravitational mass of NSs in isolation—found by a TOV solver.

To determine $\Omega^z_{\rm BNS}$ for a specific separation, we employ an iterative approach based on the force balance method described in equation (52). To validate the accuracy of the generated ID against the expected analytical values for significant separations, particularly when the BNS system exhibits quasi-circular motion, we calculate the binding energy $E_{\rm b}$ corresponding to the given $\Omega^z_{\rm BNS}$ utilizing a post-Newtonian formula , the 4 post-Newtonian order approximation, outlined in [94], section 7.4. Specifically, to compute the post-Newtonian values of $E_{\rm b}$, we need the reduced mass $\mu = M^1_{\rm TOV} M^2_{\rm TOV}/M_\infty$, the symmetric mass $\nu = \mu/M_\infty$, and the dimensionless orbital velocity $x^{3/2} = \Omega^z_{\rm BNS} M_\infty$.

Figure 4 illustrates the binding energy of the BNS system across different separations compared to the post-Newtonian data points. In cases of binaries with significant separations, meeting the quasi-circular motion criteria, we observe that the post-Newtonian and NR values align. However, for smaller separations, the NR values of $E_{\rm b}$ are marginally higher.

4.3. Spin

We generate ID for different $\Omega^z_{\rm NS}$, in equation (24), values pertaining to one of the NS in the BNS system, where each NS has a baryon mass of 1.4, and they are separated by $30M_\odot$. In this scenario, we utilize the K96 EOS. The maximum dimensionless spin achievable is $\approx$0.56,

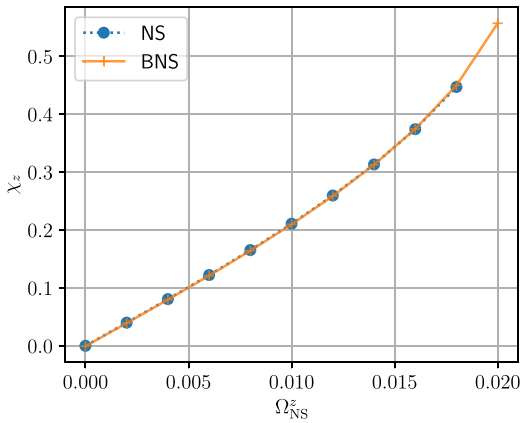

Figure 5. The relation between $\Omega^z_{\rm NS}$ and χ_z is depicted by the solid line for a symmetric mass BNS system with a baryonic mass of 1.4 and a separation of $30\,M_\odot$. The dashed line shows the corresponding values of χ_z for an isolated spinning NS for the same values of baryonic mass and EOS. We find an excellent agreement between spin values of the isolated NS and the BNS system. Initially, χ_z exhibits a linear growth pattern with $\Omega^z_{\rm NS}$, but as $\Omega^z_{\rm NS}$ is raised beyond a certain point, χ_z starts to increase non-linearly.

which corresponds to the mass shedding limit of a single NS as discussed in [95]. By increasing the $\Omega^z_{\rm NS}$ beyond 0.02, the spinning NS becomes too oblate that the NS surface finding routine fails (*Step 9* in section 3.5).

Additionally, to compare the spin values in a BNS system with those of an isolated spinning NS, we create ID for isolated NS with the same values of baryon mass, EOS, and $\Omega^z_{\rm NS}$ values (except the largest value [3]). The resulting spin values are shown in figure 5, where we find excellent agreement between spin value of the isolated NS and the BNS system.

Figure 5 shows the relation between $\Omega^z_{\rm NS}$ in equation (24) and χ_z in equation (43). There is a linear relation between $\Omega^z_{\rm NS}$ and χ_z for low values of $\Omega^z_{\rm NS}$. However, as $\Omega^z_{\rm NS}$ increases, the relationship transitions into a nonlinear pattern, causing χ_z to rise more steeply.

Moreover, figure 5 can be utilized as an approximate reference to determine the appropriate value of $\Omega^z_{\rm NS}$ corresponding to a desired spin level.

4.4. Outer boundary radius

We aim to study the effect of the outer boundary radius of the grid, where equation (20) is imposed, on the convergence behavior of the constraints and the binding energy of the system. To this end, we construct four ID sets for a symmetric non-spinning BNS system with NS baryon mass 1.4 and the tabulated SLy4 EOS each featuring a different outer boundary radius. In particular, the chosen outer boundary radii are $5\times10^4\,M_\odot$, $1\times10^5\,M_\odot$, $5\times10^5\,M_\odot$, and $1\times10^6\,M_\odot$.

We find that setting the outer boundary radius larger than $10^6\,M_\odot$, can lead to code failures due to issues with the patch finder routine in the code. This routine is essential for establishing the inter-BC [25] between adjacent patches, as it identifies neighboring patches for each patch. Consequently, additional code support would be necessary if a larger outer boundary

[3] To create ID for $\Omega^z_{\rm NS}=0.02$, the NS surface finding routine fails, hence we can not report the corresponding spin value.

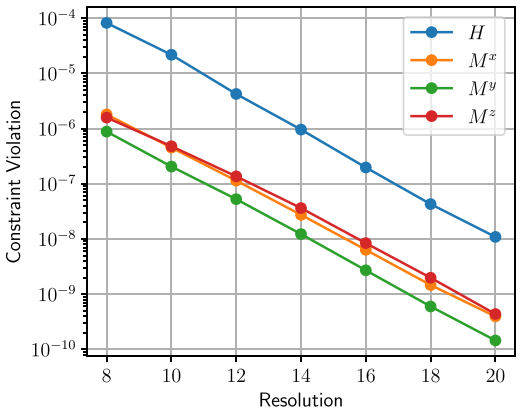

Figure 6. Shown is the L_2-norm of Hamiltonian (H) and momentum (M^i) constraint violations for a symmetric BNS system with the tabulated SLy4 EOS and the outer boundary radius of $5 \times 10^5\,\mathrm{M}_\odot$. The constraints are calculated for an arbitrary patch that covers large-radius regions of the grid, where the flat spacetime BCs, equation (20), are imposed on its outermost boundary. Other patches within these large-radius regions display a similar convergence pattern.

is required. However, a grid with an outer boundary at $10^6\,\mathrm{M}_\odot$ is already few orders of magnitude larger than the typical grids used in evolution simulations, such as those in [57, 96, 97]. Therefore, this size is sufficiently large for the ID to be interpolated onto the grid of an evolution code.

Figure 6 illustrates the convergence test of the Hamiltonian and momentum constraints focusing on one of the patches that cover the large-radius regions of the grid, i.e, reaching the outer boundary of the grid. We observe a clear spectral convergence for all constraints. This convergence behavior remains quantitatively unchanged across all other patches in these large-radius regions as well as across all other ID sets with different outer boundary radii. Furthermore, the convergence behavior for all regions, NS exterior regions, and NS interior regions are consistent with the findings for the SFHo EOS, and discussed in section 4.1.

Additionally, in figure 7, we plot the absolute value of the relative difference in binding energy as a function of the outer boundary radius. We define $\Delta E_\mathrm{b} = \bar{E}_\mathrm{b} - E_\mathrm{b}$, in which $\bar{E}_\mathrm{b}$ represents the binding energy of the BNS system with the largest outer boundary radius, namely, $10^6\,\mathrm{M}_\odot$. We observe that the relative difference in binding energy exhibits converging behavior with respect to the $\bar{E}_\mathrm{b}$ benchmark. Presuming that the largest radius provides the most accurate binding energy ($\bar{E}_\mathrm{b}$), we find the relative difference between the binding energies at smallest outer boundary radius and the largest one is $\sim 0.3\%$. Furthermore, the relative difference in binding energies between $5 \times 10^5\,\mathrm{M}_\odot$ and $1 \times 10^6\,\mathrm{M}_\odot$ radii is $\sim 0.04\%$.

These results suggest that we can construct constraint satisfying and self-consistent ID for different values of the outer boundary radius of the grid.

5. Summary

In this work we have presented a significant upgrade to the `Elliptica` infrastructure. Previously limited to black hole-NS system and (piecewise) polytropic EOS for NSs, `Elliptica` can now construct ID for spinning BNS systems, incorporating realistic tabulated EOSs for the NS matter.

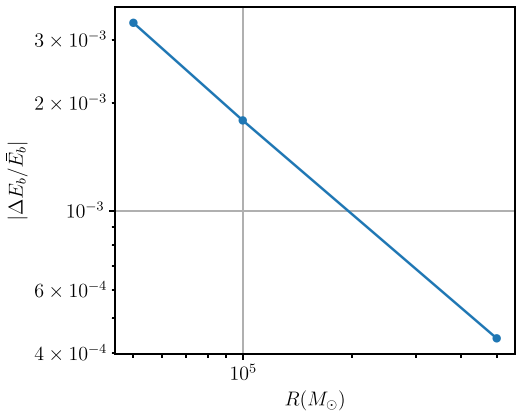

Figure 7. Relative difference in binding energy as a function of outer boundary radius. We define $\Delta E_b = \bar{E}_b - E_b$, in which $\bar{E}_b$ represents the binding energy of the BNS system with the largest outer boundary radius, i.e. $10^6\,\mathrm{M}_\odot$.

To incorporate tabular EOSs, we have developed a number of techniques centered around interpolation that allow convergence in the resulting solution while remaining as true as possible to the underlying microphysics. While the convergence of the solution is negatively affected by the complexity of the EOS, we maintain convergence up to a limit imposed by the surface features.

In this work, we selected tabulated SLy4 and SFHo EOSs from the `CompOSE` tables. Since these EOSs are generic among available cold NS EOS tables, our numerical methods remain still applicable to many such EOSs. Additionally, our conclusions regarding convergence, for example, are relevant because the limiting factors on accuracy are common across these families of EOSs.

We have validated our code through convergence tests and comparisons with established analytical results, particularly in the post-Newtonian regime. Additionally, by setting the outer boundary radius at different values, we study the convergence of the constraints and the binding energy of the system. We observe that the constraints exhibit spectral convergence in patches covering the large-radius regions of the grid. Furthermore, we find that choosing an outer boundary radius in the range of $(10^5, 10^6)\,\mathrm{M}_\odot$ results in an uncertainty bound of less than $\sim 0.2\%$ in the binding energy of the BNS system. These tests demonstrate the code's accuracy and robustness.

For smooth EOS, such as polytropic models, we achieve spectral convergence, indicating an optimal error reduction rate with increasing resolution. However, for EOS tables with discontinuities, spectral convergence is diminished. At high resolutions, we observe a convergence plateau inside NS, though global convergence is still ensured. This behavior is expected for discontinuous functions.

While we have not studied our ID in the context of an evolution simulation in this work, it is important to assess the quality of the ID after its interpolation onto the grid of an evolution code. In particular, the propagation of constraint violations and the oscillation of the rest mass density at the center of each NS are important diagnostics to be studied. Moreover, since different ID codes employ different numerical parameters and algorithms to solve ID equations, it is important to examine the effects of these differences on the resultant gravitational waves. Specifically, from the point of view of the next generation detectors such as

Cosmic Explorer [11], we need to study the mismatch between two gravitational wave signals emitted from the evolution of a BNS system started from the same ID but using two different ID codes. These topics are left for future work.

While some first steps have been taken to construct self-consistent ID for magnetized NSs by solving the Einstein–Euler–Maxwell equations assuming ideal magnetohydrodynamic [98, 99], there are no ID with self-consistent magnetic field for binary systems. As such, a particularly interesting area for future development lies in constructing self-consistent ID for BNS systems that contain magnetic fields. This capability would be specially valuable for studying systems containing pulsars or magnetars, where these fields play a significant role in the dynamics.

Data availability statement

The data that support the findings of this study are openly available at the following URL/DOI: https://github.com/rashti-alireza/Elliptica.

Acknowledgments

A R and A N gratefully acknowledge David Radice for valuable discussions and insightful feedback on the manuscript. A R acknowledges support from NASA under Award No. 80NSSC21K1720. The numerical simulations were performed on Roar Collab High Performance Computing Cluster at The Pennsylvania State University.

`Elliptica` is now public [4] and open-source under `GPL-3.0` license.

Appendix A. Interpolation of the equation of state

To generate a suitable interpolant of a tabular EOS, we first approximate $\frac{\partial p}{\partial h}$, $\frac{\partial \epsilon}{\partial h}$, and $\frac{\partial \rho_0}{\partial h}$ by finite-difference methods on the `CompOSE` data using Fornberg's algorithm [100], explained in appendix B, for unevenly-spaced grids. Having the derivatives, we then generate a spline interpolant composed of Hermite polynomials. The procedure for e.g. the pressure $p(h)$ is:

Step 0: we are given data points (p_j, h_j) monotonically increasing in h.

Step 1: for each point j, we take the set of N points $X_j = \{h_{j-\frac{N}{2}}, \ldots, h_j, \ldots, h_{j+\frac{N}{2}}\}$ centered around h_j. We shift the indices when needed for points near the boundaries h_0 and $h_{j_{\max}}$.

Step 2: at each point, approximate $\left.\frac{\mathrm{d}p}{\mathrm{d}h}\right|_{h_j} \approx \sum_{\nu=j-\frac{N}{2}}^{j+\frac{N}{2}} \delta^1_{N,\nu} p_\nu$, with the coefficients δ calculated by Fornberg's algorithm applied over the set X_j obtained in *Step 1*.

Step 3: having p_j and its derivative $\frac{\mathrm{d}p(h_j)}{\mathrm{d}h}$, we generate the interpolating Hermite polynomial (according to [101]) of desired order.

The same procedure is applied to obtain splines for $e(h)$, $\rho_0(h)$, and $\epsilon(h)$. Derivatives of these functions are thereafter approximated by analytical derivatives of the spline interpolant.

[4] https://github.com/rashti-alireza/Elliptica.

Algorithm 2. Simplification of Fornberg's finite difference algorithm, adapted from [100].

$\delta^0_{0,0} = c_1 = 1$
for $n = 1, \ldots, N$ **do**
  $c_2 = 1$
  for $\nu = 0, \ldots, n-1$ **do**
    $c_3 = x_n - x_\nu$
    $c_2 = c_2 \cdot c_3$
    if $n = 0, 1$ **then**
      $\delta^{n-1}_{n-1,\nu} = 0$
    end if
    $\delta^0_{n,\nu} = \frac{(x_n - h_j)}{c_3}\,\delta^0_{n-1,\nu}$
    $\delta^1_{n,\nu} = \frac{1}{c_3}\left((x_n - h_j)\,\delta^1_{n-1,\nu} - \delta^0_{n-1,\nu}\right)$
  end for
  $\delta^0_{n,n} = \frac{c_1}{c_2}\,(h_j - x_{n-1})\,\delta^0_{n-1,n-1}$
  $\delta^1_{n,n} = \frac{c_1}{c_2}\left(\delta^0_{n-1,n-1} + (h_j - x_{n-1})\,\delta^1_{n-1,n-1}\right)$
  $c_1 = c_2$
end for

Appendix B. Application of Fornberg's finite difference method

Step 2 of section (appendix A) entails finding derivatives such as $\frac{\mathrm{d}p}{\mathrm{d}h}$, which EOS tables do not provide. We evaluate these derivatives numerically using finite difference methods on the data points (p_j, h_j). Since the data points are typically unevenly spaced, we use Fornberg's finite difference algorithm to generate finite difference coefficients that approximate $\frac{\mathrm{d}p(h_j)}{\mathrm{d}h}$ at each point [100]. Specifically, the algorithm calculates the weights $\delta^m_{N,\nu}$ such that

$$\left.\frac{\mathrm{d}^m p}{\mathrm{d}h^m}\right|_{h_j} \approx \sum_{\nu=j-\frac{N}{2}}^{j+\frac{N}{2}} \delta^m_{N,\nu} p_\nu, \tag{B.1}$$

where N is the number of points used (and determines the order of the finite difference approximation).

While Fornberg's algorithm can provide derivatives of arbitrarily high orders (given enough data points), we are only interested in the first derivative. In addition, we do not need the finite difference coefficients for all orders, so we simplify the algorithm slightly. Then given a subset X_j centered around h_j, from *Step 1* of appendix A, we find the finite difference weights using algorithm 2 (where c_1, c_2, and c_3 are introduced just to simplify the notation, and x_k is the kth element of X_j).

ORCID iD

Alireza Rashti https://orcid.org/0000-0003-3558-7684

References

[1] Abbott B P *et al* 2020 GW190425: observation of a compact binary coalescence with total mass $3.4M_{\odot}$ *Astrophys. J. Lett.* **892** L3

[2] Chaurasia S V, Dietrich T, Johnson-McDaniel N K, Ujevic M, Tichy W and Brügmann B 2018 Gravitational waves and mass ejecta from binary neutron star mergers: effect of large eccentricities *Phys. Rev.* D **98** 104005

[3] Chaurasia S V, Dietrich T, Ujevic M, Hendriks K, Dudi R, Fabbri F M, Tichy W and Brügmann B 2020 Gravitational waves and mass ejecta from binary neutron star mergers: effect of the spin orientation *Phys. Rev.* D **102** 024087

[4] Fernández R, Tchekhovskoy A, Quataert E, Foucart F and Kasen D 2019 Long-term GRMHD simulations of neutron star merger accretion discs: implications for electromagnetic counterparts *Mon. Not. R. Astron. Soc.* **482** 3373–93

[5] Sun L, Ruiz M, Shapiro S L and Tsokaros A 2022 Jet launching from binary neutron star mergers: incorporating neutrino transport and magnetic fields *Phys. Rev.* D **105** 104028

[6] Siegel D M 2022 r-Process nucleosynthesis in gravitational-wave and other explosive astrophysical events *Nat. Rev. Phys.* **4** 306–18

[7] Fernández R and Metzger B D 2016 Electromagnetic signatures of neutron star mergers in the advanced LIGO era *Ann. Rev. Nucl. Part. Sci.* **66** 23–45

[8] Aasi J *et al* 2015 Advanced LIGO *Class. Quantum Grav.* **32** 074001

[9] Acernese F *et al* 2015 Advanced Virgo: a second-generation interferometric gravitational wave detector *Class. Quantum Grav.* **32** 024001

[10] Akutsu T *et al* 2021 Overview of KAGRA: calibration, detector characterization, physical environmental monitors and the geophysics interferometer *Prog. Theor. Exp. Phys.* **2021** 05A102

[11] Reitze D *et al* 2019 Cosmic explorer: the U.S. contribution to gravitational-wave astronomy beyond LIGO *Bull. Am. Astron. Soc.* **51** 035

[12] Kawamura S *et al* 2021 Current status of space gravitational wave antenna DECIGO and B-DECIGO *PTEP* **2021** 05A105

[13] Punturo M *et al* 2010 The Einstein telescope: a third-generation gravitational wave observatory *Class. Quantum Grav.* **27** 194002

[14] Adhikari R X *et al* 2019 Astrophysical science metrics for next-generation gravitational-wave detectors *Class. Quantum Grav.* **36** 245010

[15] Amaro-Seoane P *et al* 2017 Laser interferometer space antenna (arXiv:1702.00786)

[16] Ackley K *et al* 2020 Neutron star extreme matter observatory: a kilohertz-band gravitational-wave detector in the global network *Publ. Astron. Soc. Austral.* **37** e047

[17] Luo J *et al* 2016 TianQin: a space-borne gravitational wave detector *Class. Quantum Grav.* **33** 035010

[18] Abbott B P *et al* 2017 GW170817: observation of gravitational waves from a binary neutron star inspiral *Phys. Rev. Lett.* **119** 161101

[19] Abbott B P *et al* 2017 Gravitational waves and gamma-rays from a binary neutron star merger: GW170817 and GRB 170817A *Astrophys. J. Lett.* **848** L13

[20] Coulter D A *et al* 2017 Swope supernova survey 2017a (SSS17a), the optical counterpart to a gravitational wave source *Science* **358** 1556

[21] Foucart F, Laguna P, Lovelace G, Radice D and Witek H 2022 Snowmass2021 cosmic frontier white paper: numerical relativity for next-generation gravitational-wave probes of fundamental physics

[22] Uryu K and Tsokaros A 2012 A new code for equilibriums and quasiequilibrium initial data of compact objects *Phys. Rev.* D **85** 064014

[23] Tsokaros A, Uryū K and Rezzolla L 2015 New code for quasiequilibrium initial data of binary neutron stars: corotating, irrotational and slowly spinning systems *Phys. Rev.* D **91** 104030

[24] Boukas L, Tsokaros A and Uryu K 2023 The parallel compact object calculator: an efficient general relativistic initial data solver for compact objects

[25] Rashti A, Fabbri F M, Brügmann B, Chaurasia S V, Dietrich T, Ujevic M and Tichy W 2022 New pseudospectral code for the construction of initial data *Phys. Rev.* D **105** 104027

[26] Papenfort L J, Tootle S D, Grandclément P, Most E R and Rezzolla L 2021 New public code for initial data of unequal-mass, spinning compact-object binaries *Phys. Rev.* D **104** 024057

[27] Lorene Langage objet pour la relativité numériquE

[28] Philippe G 2006 Accurate and realistic initial data for black hole-neutron star binaries *Phys. Rev.* D **74** 124002
Philippe G 2007 *Phys. Rev.* D **75** 129903 (erratum)
[29] Taniguchi K, Baumgarte T W, Faber J A and Shapiro S L 2006 Quasiequilibrium sequences of black-hole-neutron-star binaries in general relativity *Phys. Rev.* D **74** 041502
[30] Taniguchi K, Baumgarte T W, Faber J A and Shapiro S L 2007 Quasiequilibrium black hole-neutron star binaries in general relativity *Phys. Rev.* D **75** 084005
[31] Taniguchi K, Baumgarte T W, Faber J A and Shapiro S L 2008 Relativistic black hole-neutron star binaries in quasiequilibrium: effects of the black hole excision boundary condition *Phys. Rev.* D **77** 044003
[32] Assumpcao T, Werneck L R, Pierre Jacques T and Etienne Z B 2022 Fast hyperbolic relaxation elliptic solver for numerical relativity: conformally flat, binary puncture initial data *Phys. Rev.* D **105** 104037
[33] Tichy W 2009 A New numerical method to construct binary neutron star initial data *Class. Quantum Grav.* **26** 175018
[34] Tichy W 2012 Constructing quasi-equilibrium initial data for binary neutron stars with arbitrary spins *Phys. Rev.* D **86** 064024
[35] Tichy W, Rashti A, Dietrich T, Dudi R and Brügmann B 2019 Constructing binary neutron star initial data with high spins, high compactnesses and high mass ratios *Phys. Rev.* D **100** 124046
[36] Fischer N L and Pfeiffer H P 2022 Unified discontinuous Galerkin scheme for a large class of elliptic equations *Phys. Rev.* D **105** 024034
[37] Vu N L *et al* 2022 A scalable elliptic solver with task-based parallelism for the SpECTRE numerical relativity code *Phys. Rev.* D **105** 084027
[38] Pfeiffer H P, Kidder L E, Scheel M A and Teukolsky S A 2003 A Multidomain spectral method for solving elliptic equations *Comput. Phys. Commun.* **152** 253–73
[39] Foucart F, Kidder L E, Pfeiffer H P and Teukolsky S A 2008 Initial data for black hole-neutron star binaries: a flexible, high-accuracy spectral method *Phys. Rev.* D **77** 124051
[40] Tacik N *et al* 2015 Binary neutron stars with arbitrary spins in numerical relativity *Phys. Rev.* D **92** 124012
Tacik N *et al* 2016 *Phys. Rev.* D **94** 049903 (erratum)
[41] Tacik N, Foucart F, Pfeiffer H P, Muhlberger C, Kidder L E, Scheel M A and Szilágyi B 2016 Initial data for black hole–neutron star binaries, with rotating stars *Class. Quantum Grav.* **33** 225012
[42] Ansorg M, Bruegmann B and Tichy W 2004 A Single-domain spectral method for black hole puncture data *Phys. Rev.* D **70** 064011
[43] Ansorg M 2005 A Double-domain spectral method for black hole excision data *Phys. Rev.* D **72** 024018
[44] Zhu H, Fields J, Zappa F, Radice D, Stone J, Rashti A, Cook W, Bernuzzi S and Daszuta B 2024 Performance-portable numerical relativity with Athenak
[45] Fields J, Zhu H, Radice D, Stone J M, Cook W, Bernuzzi S and Daszuta B 2024 Performance-portable binary neutron star mergers with Athenak
[46] Bruegmann B, Gonzalez J A, Hannam M, Husa S, Sperhake U and Tichy W 2008 Calibration of moving puncture simulations *Phys. Rev.* D **77** 024027
[47] Thierfelder M, Bernuzzi S and Bruegmann B 2011 Numerical relativity simulations of binary neutron stars *Phys. Rev.* D **84** 044012
[48] Dietrich T, Bernuzzi S, Ujevic M and Brügmann B 2015 Numerical relativity simulations of neutron star merger remnants using conservative mesh refinement *Phys. Rev.* D **91** 124041
[49] Bugner M, Dietrich T, Bernuzzi S, Weyhausen A and Brügmann B 2016 Solving 3D relativistic hydrodynamical problems with weighted essentially nonoscillatory discontinuous Galerkin methods *Phys. Rev.* D **94** 084004
[50] Hilditch D, Weyhausen A and Brügmann B 2016 Pseudospectral method for gravitational wave collapse *Phys. Rev.* D **93** 063006
[51] Renkhoff S, Cors D, Hilditch D and Brügmann B 2023 Adaptive hp refinement for spectral elements in numerical relativity *Phys. Rev.* D **107** 104043
[52] Fernando M, Neilsen D, Lim H, Hirschmann E and Sundar H 2018 Massively parallel simulations of binary black hole intermediate-mass-ratio inspirals
[53] Löffler F *et al* 2012 The einstein toolkit: a community computational infrastructure for relativistic astrophysics *Class. Quantum Grav.* **29** 115001

[54] Haas R *et al* 2020 The einstein toolkit To find out more, visit (available at: http://einsteintoolkit. org)
[55] Köppel S 2018 Towards an exascale code for GRMHD on dynamical spacetimes *J. Phys.: Conf. Ser.* **1031** 012017
[56] Daszuta B, Zappa F, Cook W, Radice D, Bernuzzi S and Morozova V 2021 GR-Athena++: puncture evolutions on vertex-centered oct-tree adaptive mesh refinement *Astrophys. J. Supp.* **257** 25
[57] Cook W, Daszuta B, Fields J, Hammond P, Albanesi S, Zappa F, Bernuzzi S and Radice D 2023 GR-Athena++: general-relativistic magnetohydrodynamics simulations of neutron star spacetimes
[58] Rashti A, Bhattacharyya M, Radice D, Daszuta B, Cook W and Bernuzzi S 2024 Adaptive mesh refinement in binary black holes simulations *Class. Quantum Grav.* **41** 095001
[59] Shankar S, Mösta P, Brandt S R, Haas R, Schnetter E and de Graaf Y 2022 GRaM-X: a new GPU-accelerated dynamical spacetime GRMHD code for exascale computing with the Einstein toolkit
[60] Schnetter E, Brandt S, Cupp S, Haas R, Möstaand P and Shankar S 2022 CarpetX for the Einstein toolkit (*Zenodo*) (https://doi.org/10.5281/zenodo.6131529)
[61] Clough K, Figueras P, Finkel H, Kunesch M, Lim E A and Tunyasuvunakool S 2015 GRChombo : numerical relativity with adaptive mesh refinement *Class. Quantum Grav.* **32** 245011
[62] Andrade T *et al* 2021 GRChombo: an adaptable numerical relativity code for fundamental physics *J. Open Source Softw.* **6** 3703
[63] Tichy W, Ji L, Adhikari A, Rashti A and Pirog M 2023 The new discontinuous Galerkin methods based numerical relativity program Nmesh *Class. Quantum Grav.* **40** 025004
[64] Ruchlin I, Etienne Z B and Baumgarte T W 2018 SENR/NRPy+: numerical relativity in singular curvilinear coordinate systems *Phys. Rev.* D **97** 064036
[65] Kiuchi K, Kawaguchi K, Kyutoku K, Sekiguchi Y and Shibata M 2020 Sub-radian-accuracy gravitational waves from coalescing binary neutron stars in numerical relativity. II. Systematic study on the equation of state, binary mass and mass ratio *Phys. Rev.* D **101** 084006
[66] Palenzuela C, Miñano B, Viganò D, Arbona A, Bona-Casas C, Rigo A, Bezares M, Bona C and Massó J 2018 A Simflowny-based finite-difference code for high-performance computing in numerical relativity *Class. Quantum Grav.* **35** 185007
[67] Okounkova M 2019 Stability of rotating black holes in Einstein dilaton Gauss-Bonnet gravity *Phys. Rev.* D **100** 124054
[68] Boyle M *et al* 2019 The SXS collaboration catalog of binary black hole simulations *Class. Quantum Grav.* **36** 195006
[69] Kidder L E *et al* 2017 SpECTRE: a task-based discontinuous Galerkin code for relativistic astrophysics *J. Comput. Phys.* **335** 84–114
[70] Deppe N *et al* 2022 Simulating magnetized neutron stars with discontinuous Galerkin methods *Phys. Rev.* D **105** 123031
[71] Rosswog S and Diener P 2021 SPHINCS_BSSN: a general relativistic smooth particle hydrodynamics code for dynamical spacetimes *Class. Quantum Grav.* **38** 115002
[72] Typel S, Oertel M and Klähn T 2015 CompOSE CompStar online supernova equations of state harmonising the concert of nuclear physics and astrophysics compose.obspm.fr *Phys. Part. Nucl.* **46** 633–64
[73] Typel S *et al* 2022 CompOSE reference manual *Eur. Phys. J.* A **58** 221
[74] Oertel M, Hempel M, Klähn T and Typel S 2017 Equations of state for supernovae and compact stars *Rev. Mod. Phys.* **89** 015007
[75] York Jr J W 1999 Conformal 'thin sandwich' data for the initial-value problem *Phys. Rev. Lett.* **82** 1350–3
[76] Pfeiffer H P and York Jr J W 2003 Extrinsic curvature and the Einstein constraints *Phys. Rev.* D **67** 044022
[77] Read J S, Lackey B D, Owen B J and Friedman J L 2009 Constraints on a phenomenologically parameterized neutron-star equation of state *Phys. Rev.* D **79** 124032
[78] Gourgoulhon E 2007 3+1 formalism and bases of numerical relativity
[79] Rezzolla L and Zanotti O 2013 *Relativistic Hydrodynamics* (Oxford University Press)
[80] Ronchi C, Iacono R and Paolucci P S 1996 The "cubed sphere": a new method for the solution of partial differential equations in spherical geometry *J. Comput. Phys.* **124** 93–114
[81] Saad Y 2003 *Iterative Methods for Sparse Linear Systems (Society for Industrial and Applied Mathematics)* (SIAM)

[82] Davis T A 2004 Algorithm 832: UMFPACK V4.3 - an unsymmetric-pattern multifrontal method *ACM Trans. Math. Softw.* **30** 196–9
[83] Gourgoulhon E 2011 *3 + 1 Formalism in General Relativity* (Springer)
[84] Campanelli M, Lousto C O, Zlochower Y, Krishnan B and Merritt D 2007 Spin flips and precession in black-hole-binary mergers *Phys. Rev.* D **75** 064030
[85] Steiner A W, Hempel M and Fischer T 2013 Core-collapse supernova equations of state based on neutron star observations *Astrophys. J.* **774** 17
[86] O'Boyle M F, Markakis C, Stergioulas N and Read J S 2020 Parametrized equation of state for neutron star matter with continuous sound speed *Phys. Rev.* D **102** 083027
[87] Lindblom L 2010 Spectral representations of neutron-star equations of state *Phys. Rev.* D **82** 103011
[88] Foucart F, Duez M D, Gudinas A, Hebert F, Kidder L E, Pfeiffer H P and Scheel M A 2019 Smooth equations of state for high-accuracy simulations of neutron star binaries *Phys. Rev.* D **100** 104048
[89] Baumgarte T W and Shapiro S L 2010 *Numerical Relativity: Solving Einstein's equations on the Computer* (Cambridge University Press)
[90] Haensel P, Zdunik J L and Douchin F 2002 Equation of state of dense matter and the minimum mass of cold neutron stars *Astron. Astrophys.* **385** 301
[91] Boyd J P 2001 *Chebyshev and Fourier Spectral Methods* (Dover Publications)
[92] Lindblom L 2022 Improved spectral representations of neutron-star equations of state *Phys. Rev.* D **105** 063031
[93] Tichy W 2017 The initial value problem as it relates to numerical relativity *Rep. Prog. Phys.* **80** 026901
[94] Blanchet L 2014 Gravitational radiation from post-newtonian sources and inspiralling compact binaries *Living Rev. Relativ.* **17** 2
[95] Ansorg M, Kleinwachter A and Meinel R 2003 Highly accurate calculation of rotating neutron stars: detailed description of the numerical methods *Astron. Astrophys.* **405** 711
[96] Ujevic M, Rashti A, Gieg H, Tichy W and Dietrich T 2022 High-accuracy high-mass-ratio simulations for binary neutron stars and their comparison to existing waveform models *Phys. Rev.* D **106** 023029
[97] Bernuzzi S, Magistrelli F, Jacobi M, Logoteta D, Perego A and Radice D 2024 Long-lived neutron-star remnants from asymmetric binary neutron star mergers: element formation, kilonova signals and gravitational waves
[98] Gourgoulhon E, Markakis C, Uryu K and Eriguchi Y 2011 Magnetohydrodynamics in stationary and axisymmetric spacetimes: a fully covariant approach *Phys. Rev.* D **83** 104007
[99] Tsokaros A, Ruiz M, Shapiro S L and Uryū K 2022 Magnetohydrodynamic simulations of self-consistent rotating neutron stars with mixed poloidal and toroidal magnetic fields *Phys. Rev. Lett.* **128** 061101
[100] Fornberg B 1988 Generation of finite difference formulas on arbitrarily spaced grids *Math. Comput.* **51** 699–706
[101] Burden R L and Douglas Faires J 2011 *Numerical Analysis* 9th edn (Brooks/Cole)